Journal of
Materials Chemistry B

ROYAL SOCIETY
OF CHEMISTRY

PAPER

View Article Online
View Journal | View Issue

Check for updates

Cite this: *J. Mater. Chem. B*, 2026, **14**, 3703

Synthesis and characterization of an injectable telechelic material for the epiretinal delivery of retinal gene therapies

James H. Westbay,[a] Daniel P. Bigley,[a] Sushma Sappa,[a] Anfisa Ayalon,[a] Hamzah Aweidah,[a] Lauren D. Dignam,[a] Joseph N. Martel,[a] William A. Beltran,[b] José-Alain Sahel,[ac] Leah C. Byrne[ade] and Morgan V. DiLeo*[aefg]

Received 2nd February 2026,
Accepted 22nd February 2026

DOI: 10.1039/d6tb00267f

rsc.li/materials-b

There is a need to develop safer, more efficient, and targeted strategies for the delivery of retinal gene therapies. Current strategies may require high dose therapeutics administered intravitreally or complex subretinal surgical delivery with increased risks. An optimized material carrier could enable localized delivery of therapeutics without extensive surgery. Here, we report a novel material carrier formed by octadecane-poly(ethylene glycol)-octadecane (OPO) molecules. OPO molecules were synthesized *via* a Williamson reaction. In aqueous solution, the octadecane heads associate to form a telechelic network. We extensively characterized this material using a variety of rheological and spectroscopic techniques. At both room temperature and body temperature, the material is a viscoelastic fluid that exhibits Maxwellian behavior. It is transparent, injectable, and spreadable without fragmentation. Delivery agents can be facilely loaded into the material as the OPO network forms. In bulk solution, the network dissolves, releasing loaded agents over a period of ∼60 min. Placement of an unloaded backing layer next to a loaded layer promotes release from the network in a targeted direction. We additionally prepared OPO loaded with adeno-associated viruses (AAVs) and demonstrated that AAV titre is homogeneously distributed throughout the material, is stable for up to 3 days, and that AAVs administered in OPO are able to transduce ARPE-19 cells. We hypothesize these properties well-position OPO as an efficient carrier to deliver retinal gene therapies, and in particular AAV vectors, *in vivo* and may prove useful in other delivery applications. This is the first report of an injectable material that can be facilely loaded with retinal gene therapies. The results presented here are a crucial preliminary step in advancing a materials-based strategy for administering gene therapies to the retina.

1. Introduction

The development of minimally invasive delivery strategies at the appropriate cell or locus of pathology, and at the appropriate dose, will improve the efficacy and safety of numerous medical treatments, including drug, cell, and gene therapies. In particular, current retinal gene therapy approaches are often inefficient and carry associated risks, such as poor localization, inefficient transduction, risks of collateral damage to healthy tissue, and immunogenicity.[1,2] Strategies for administering retinal gene therapies include intravitreal, subretinal, and suprachoroidal applications, as shown in Fig. 1. Intravitreal injections require high dosing due to the long diffusion distance of target tissue from the application site, broad intraocular exposure with high risk of intraocular inflammation, and the need to transverse several potential barriers (vitreous, internal limiting membrane, and cellular adhesion molecules) before reaching the target tissue.[3–7] Subretinal injections require the surgical induction of a neurosensory retinal detachment with limitations on volume of therapeutic agent, a risk of formation of macular holes and injection-site retinal atrophy as well as recent concern for progressive cellular atrophy.[8–11] Suprachoroidal

---

[a] *Department of Ophthalmology, University of Pittsburgh, Pittsburgh, Pennsylvania 15219, USA. E-mail: morgandileo@pitt.edu*

[b] *Division of Experimental Retinal Therapies, Department of Clinical Sciences & Advanced Medicine, School of Veterinary Medicine, University of Pennsylvania, Philadelphia, Pennsylvania 19104, USA*

[c] *Vision Institute, University of Pittsburgh Medical Center, Pittsburgh, Pennsylvania 15219, USA*

[d] *Department of Neurobiology, University of Pittsburgh, Pittsburgh, Pennsylvania 15219, USA*

[e] *Department of Bioengineering, University of Pittsburgh, Pittsburgh, Pennsylvania 15219, USA*

[f] *Department of Chemical Engineering, University of Pittsburgh, Pittsburgh, Pennsylvania 15219, USA*

[g] *McGowan Institute for Regenerative Medicine, University of Pittsburgh, Pittsburgh, Pennsylvania 15219, USA*

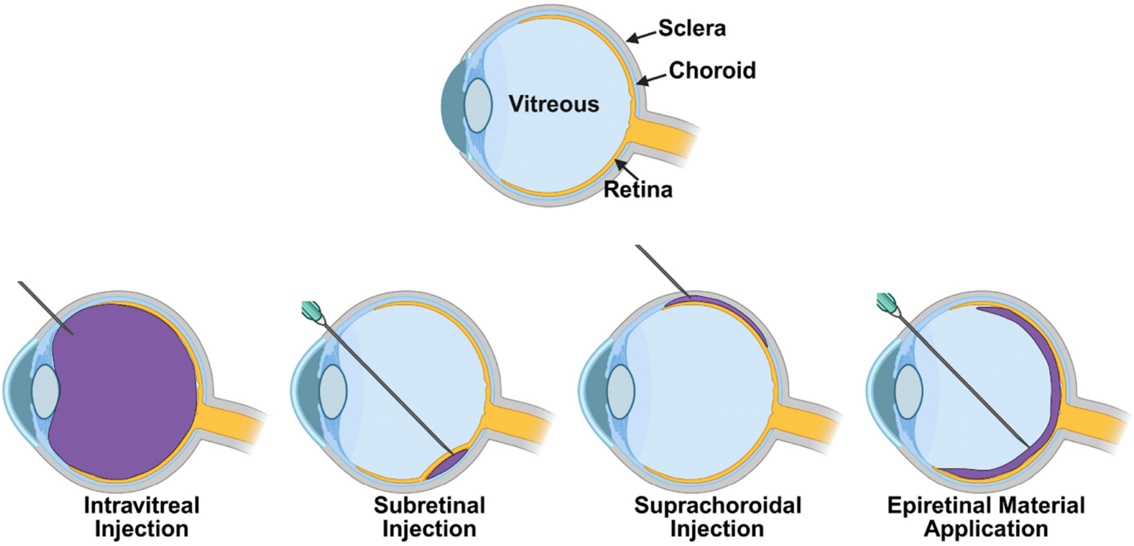

Fig. 1 Strategies for delivering retinal gene therapies. A diagram of the eye with the retina (gold), vitreous, choroid, and sclera labelled is provided for reference. Delivered therapeutics are depicted in purple. Through intravitreal injection, therapeutics are injected directly into the vitreous. Through subretinal injection, the neurosensory retina is detached, and therapeutics are delivered in the subretinal space. Through suprachoroidal injection, therapeutics are injected in the potential space between the choroid and sclera. In contrast, an injectable material carrier that is loaded with therapeutics can be applied directly onto the epiretinal surface negating the need to penetrate and detach the retina.

injections are a relatively novel strategy currently undergoing clinical trials for retinal gene therapy and cell-based therapies. While requiring further investigation, this administration strategy could suffer from rapid clearance by the choriocapillaris, immunogenicity, higher systemic absorption of gene therapy vectors, and limited posterior localization of the therapy towards the macular zone.[12,13]

Material-based delivery strategies offer improvements to these shortcomings. Materials formed by polymer networks can both retain and release loaded substances, enabling their use as platforms to deliver therapeutics. An ideal delivery platform is a nontoxic, biocompatible material that protects the loaded therapeutic agent until it is released in a target area of the body, and then is degraded without causing a severe immunogenic response. For the delivery of retinal gene therapies, an ideal platform is biocompatible, biodegradable, easily loadable, injectable, and adhesive, enabling facile and minimally invasive application onto the retinal surface without carrier material degradation byproducts.

Covalently crosslinked hydrogels are a type of polymer network that have been widely applied to the delivery of medical therapeutics.[1,14–19] When the binding energies of the covalent linkages exceed thermal fluctuations, the network structure is permanent, resulting in a static network that is mechanically robust and long-lasting.[20] While these properties enable sustained release over long periods of time,[21,22] they are detrimental to certain delivery applications. For example, covalent hydrogels may retain their shape, preventing the spread of therapeutics over the entire target area.[17] Furthermore, the mechanical properties of these hydrogels can undergo irreversible changes after injection through a syringe,[23,24] limiting methods for introduction *in vivo*.

Associative polymer networks are a type of polymer network formed by interactions that break and reform. These reversible linkages offer improvements to some of the shortcomings of covalent networks. Kato *et al.* recently reported using a poly(ethylene glycol)-based network with reversible linkages, dubbed a ‘‘slime’’, to deliver gene therapies for the treatment of skin ulcers.[17] They found that, unlike materials with static networks, the shape of the slime was malleable and could be spread over the entire area of the ulcer. They further observed that the slime enhanced localized delivery to the target superficial skin layer with fewer off-target effects compared to delivery strategies that utilized pure buffer or a gel with irreversible linkages. While a promising step in the advancement of materials-based strategies for delivering gene therapies, the material reported by Kato *et al.* does not retain loaded agents after injection and thus is not well-positioned to deliver therapeutics to the retina.[17]

While Kato *et al.* warned that injection of low-viscosity materials through a syringe can cause bursting and premature release of loaded therapeutics, other groups have reported that delivery platforms with reversible linkages do not burst on injection.[25–27] Associative networks with reversible linkages are more injectable than static networks because they can fluidize and then retain their mechanical properties after injection without fragmentation.[28,29] This enables reversible networks to retain loaded therapeutics after injection.

Wormlike micelles are a subset of associative polymer networks with reversible linkages. The networks are formed when the concentration of micelle-forming molecules reaches a critical point, causing the micelles to become entangled in a three-dimensional, wormlike structure.[30,31] A similar network can be formed by telechelic polymers containing a hydrophilic body capped by hydrophobic end groups. As the concentration of the telechelic polymer increases, the individual micelles become linked, forming an associative network. These micellular networks can be classified as either gels[32,33] or viscoelastic fluids[20,34] depending on their mechanical properties. The complex, tunable properties of telechelic networks have been of interest to basic researchers for decades.[20,35–38] Recently, telechelic materials have been proposed as a delivery platform for therapeutics.[25,39,40]

In this work, we report the development of a novel telechelic material formed by the association of octadecane-poly(ethylene glycol)-octadecane (OPO) molecules. OPO is a biocompatible, chemically inert polymer that was initially proposed as a vitreous substitute and has demonstrated compatibility with the intraocular environment.[32] Since this initial report, other poly(ethylene glycol)-based materials have been evaluated for vitreous substitution[41] and have been safely administered to the eye without adverse side effects.[42] Here, we refine the synthesis of OPO and investigate its efficacy as a delivery platform. Characterization and preliminary experiments suggest that OPO materials are promising candidates for *in vivo* delivery applications. We further observed that the OPO material described herein is sterile, injectable, and adhesive, ideally positioning it for the delivery of retinal gene therapies.

2. Experimental

2.1. Materials

Poly(ethylene glycol) (10 kDa, $Đ = 1.04$), 1,4-dioxane (anhydrous, 99.8%), toluene (anhydrous, 99.8%), sodium bicarbonate, and fluorescein isothiocyanate-dextran (FITC-dextran, 2 MDa) were purchased from Sigma-Aldrich. Sodium hydride (57–63% oil dispersion), methylene chloride, diethyl ether (anhydrous), 1X phosphate buffered saline (PBS, pH 7.4), and silica gel (0.035–0.070 mm) were purchased from Thermo Fisher Scientific. 1-Bromooctadecane (96%) was purchased from Acros Organics. Hydrochloric acid was purchased from Supelco. Ultrapure water (18.2 mΩ cm) obtained from a Milli-Q Reference A+ was used for all experiments. Vacuum filters (nylon, 0.2 μm pore size) were purchased from Corning. All chemicals were used as received unless otherwise noted.

2.2. Synthesis and characterization of OPO

2.2.1. OPO synthesis and purification. Prior to synthesis, poly(ethylene glycol) (50 g) was frozen and lyophilized for 24 h.

Scheme 1 shows the Williamson reaction used to synthesize OPO. Our synthetic method was modified from that reported by Annaka *et al.*[32] Briefly, in a Schlenk line under nitrogen, dried poly(ethylene glycol) (50 g; 50 mmol) was dissolved in dry 1,4-dioxane (150 mL) by stirring in a bath of warm tap water (∼40 °C) for 30 min. Sodium hydride (2.05 g; 50 mmol) was added portion wise, and the mixture was stirred for 1 h. Meanwhile, 1-bromooctadecane (16.6 g; 50 mmol) was dissolved in dry 1,4-dioxane (40 mL) under nitrogen. After 1 h, the bromooctadecane solution was added dropwise *via* cannula to the poly(ethylene glycol) solution. The reaction flask was stirred for 20 h at room temperature under nitrogen.

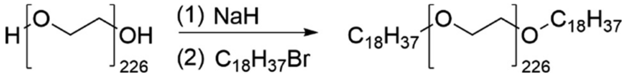

Scheme 1 Synthesis of OPO.

After 20 h, the crude reaction mixture was removed from the Schlenk line and was precipitated dropwise into diethyl ether (16 mL crude mixture:500 mL ether). The precipitate was collected as a white solid *via* vacuum filtration and dried for 3 days under vacuum. After 3 days, the dried solid was dissolved in methylene chloride (100 mL) and acid-extracted with HCl (1N; 3 × 25 mL). The organic phase was neutralized by washing with sodium bicarbonate (5% in water; 3 × 25 mL). The organic phase was further purified *via* column chromatography. A silica gel column was prepared using diethyl ether, and the crude product was loaded onto the column. Impurities were removed *via* elution with diethyl ether. The desired OPO product was then eluted with methylene chloride, dried, and isolated as a white powder.

2.2.2. OPO sterilization. To sterilize OPO, a 5% OPO solution was prepared in water. The solution was passed through a 0.2 μM Nylon filter. In a sterile environment, the filtered solution was distributed into sterile conical tubes, frozen in liquid nitrogen, and lyophilized. The sterile OPO was recovered as a white powder.

To verify sterility, OPO was incubated in tryptic soy broth and fluid thioglycollate media at 37 °C. The OPO was deemed sterile if no growth was observed after 2 weeks of incubation.

2.2.3. NMR. ^{1}H NMR spectra were acquired in $CDCl_3$ (10 mg mL^{-1}) using a 300 MHz Bruker Advance NMR spectrometer.

2.2.4. Size-exclusion chromatography (SEC). SEC was carried out on a TOSOH HLC-8320GPC EcoSEC equipped with a TSKgel-G3000H column. Measurements were carried out at room temperature with THF mobile phase. Samples were prepared in THF (10 mg mL^{-1}). M_{n}, M_{w}, and $Đ$ were determined using a refractive index detector (TOSOH) through comparison to poly(styrene) standards (2.5, 5, 9, 30, 50 and 90 kDa).

2.2.5. FTIR-ATR. IR spectra were collected using a Nicolet iS50 FTIR Spectrometer (Thermo Scientific) with a diamond crystal for single-bounce attenuated total reflectance sampling. Each sample was analysed as a solid and scanned 64 times over a range of 4000–450 cm^{-1}. Spectra were normalized by dividing each absorbance measurement by the maximum absorbance value.

2.3. Preparation and characterization of telechelic network formed by OPO

2.3.1. Preparation of telechelic network using OPO. Telechelic networks were prepared by resuspending OPO in aqueous solution, as shown in Fig. 2A. OPO was diluted to the desired concentration in either a conical tube or a syringe and then spun at 1811 RCF for 90 min on a 5810 R centrifuge.

To prepare loaded OPO material, loading agent was added to the resuspension buffer. After centrifugation, the loading agent

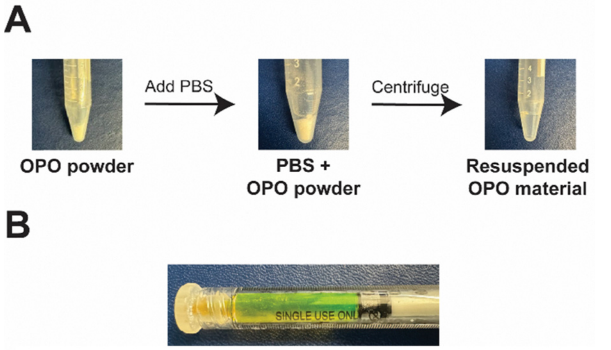

Fig. 2 (A) Preparation of OPO telechelic network. After synthesis, purification, and sterilization, OPO was stored as a white powder under vacuum. To fabricate the OPO network, OPO powder was placed in a tube and diluted with PBS to the desired OPO concentration. The mixture was then centrifuged for 90 min, yielding a transparent material. (B) OPO material loaded with FITC-dextran dye. To prepare loaded OPO material, loading agent was added to the PBS used to resuspend the telechelic network.

became trapped throughout the telechelic OPO network. Fig. 2B shows an example of OPO loaded with FITC-dextran dye.

2.3.2. Rheology. Rheological measurements were performed using an Anton Paar MCR 302 rheometer with 25 mm parallel plates and a 0.5 mm gap. Frequency sweep measurements were performed with shear amplitude $\gamma = 1\%$, and an oscillating frequency of 0.1–100 s^{-1}. Shear rate measurements were performed with a logarithmic ramp of 0.1–100 s^{-1}. Measurements were conducted at room temperature, unless otherwise noted. For measurements conducted at 38 °C, the instrument geometry was preheated to 38 °C for >15 min.

2.4. Dissolution and release assays

2.4.1. Dissolution assay. OPO networks (500 μL; 14% in 1X PBS) were prepared as described in Section 2.3.1. The network was manually injected through an 18G needle onto the bottom of a scintillation vial and incubated in 5 mL of 1X PBS. The sample was gently agitated on a mixer (250 rpm). An aliquot (100 μL) was removed from the bulk solution at t = 0, 2, 4, 6, 8, 10, 20, 30, 40, 50, 60, 90, 120, 150, and 180 min, and after 24 h. The concentration of OPO was determined by measuring absorbance on a SpectraMax M4 (Molecular Devices, Sunnyvale, Cal; 215 nm) microplate reader and comparing to an external calibration curve (see SI for calibration curve). Each measurement was repeated 3 times (n = 3).

2.4.2. Release assays. OPO networks (500 μL; 14%) were loaded with FITC-dextran dye by resuspending in 20 mg mL^{-1} FITC-dextran solutions, as described in Section 2.3.1. The loaded network was manually injected through an 18G needle onto the bottom of a scintillation vial and incubated in 5 mL of 1X PBS. Agitated samples were placed on a mixer (250 rpm). Samples with no agitation were gently swirled before aliquoting. For samples at 37 °C, the buffer and mixer were prewarmed in an incubator for 30 min, and samples remained in the incubator for the duration of the experiment. An aliquot (100 μL) was removed from the bulk solution at t = 0, 2, 4, 6, 8, 10, 20, 30, 40, 50, 60, 90, 120, 150, and 180 min, and after 24 h. The concentration of FITC-dextran was determined by measuring fluorescence on a SpectraMax M4 (Molecular Devices, Sunnyvale, Cal; ex = 490 nm, em = 520 nm) microplate reader and comparing to an external calibration curve (see SI for calibration curve). Each measurement was repeated 3 times (n = 3).

2.5. OPO backing layer

Fig. 3 shows the custom two-chamber setup we designed to evaluate the impact of an unloaded OPO backing layer on release of loaded agents from the OPO network. A cylindrical cell (inner diameter = 4 mm) (Fig. 3A and B) was connected to two chambers *via* Luer-lock T-junctions (Fig. 3C).

OPO loaded with FITC-dextran dye and unloaded OPO were prepared using the methodology described in Section 2.3.1. Loaded OPO (100 μL) was manually injected through an 18G needle into one half of the cylindrical cell. Unloaded OPO (100 μL) was manually injected through an 18G needle into the opposing half, such that the loaded and unloaded layers were touching, and each layer faced an opposing window of the cell. Each face of the cell was then attached to a different chamber *via* a T-junction. 1X PBS (2.5 mL in each chamber, 5 mL total) was added into either chamber. The entire setup was placed on a shaker and gently agitated at 100 rpm. An aliquot (100 μL) was removed from each chamber for every 30 min over a 4 h period, and then again after 72 h. Fluorescence was measured using a SpectraMax M4 (Molecular Devices, Sunnyvale, Cal; ex = 490 nm, em = 520 nm) microplate reader. For each time point, mass of FITC-dextran dye was calculated by comparison to an external calibration curve (see SI for calibration curve). Relative mass was calculated by dividing the mass of FITC-dextran dye in each chamber at each time point by the sum of masses in both chambers after 72 h. Each measurement was repeated 3 times (n = 3).

2.6. Stability and distribution of AAVs in OPO network

For these studies, AAVs (K912-CAG-mGL-BC29) were purchased from PackGene. Prior to shipment, AAVs were characterized using transmission electron microscopy, SDS-PAGE, SYBR

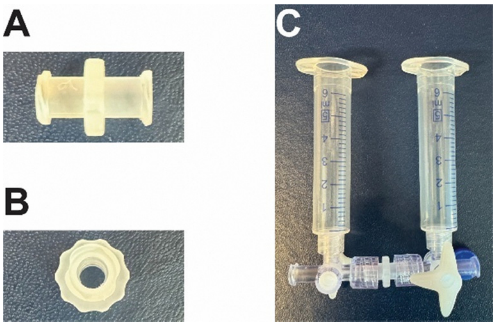

Fig. 3 Backing layer experimental setup. (A) Side view and (B) top view of the sample cell that the OPO material was injected into. (C) The full, two-chambered set up. The sample cell was positioned between each chamber by a T-junction. Buffer passed from chamber to chamber through the sample cell.

Green qPCR, ddPCR, and capillary electrophoresis. AAVs were additionally tested for mycoplasma and thermophilic bacteria and fungi. All AAVs were stored in 1X PBS (pH 7.4) without any additives.

2.6.1. AAV stability assay. AAV-loaded OPO samples were prepared in syringes as described in Section 2.3.1. A sample from the loaded syringe was immediately collected into an Eppendorf tube, designated as $t = 0$ h, and stored at −80 °C. The remaining syringe samples were stored at 4 °C between collections. Subsequent aliquots were collected at $t = 24$–48, 48–72, and 144 h. Immediately before analysis, the collected AAV-loaded OPO samples were thawed at room temperature and subsequently heated to 95 °C until the OPO fluidized (5–10 min). An aliquot (2 μL) from each sample was analysed to evaluate the final AAV titre using a qPCR AAV Titre Kit (Applied Biological Materials Inc, Cat. No. G931) that targets the AAV inverted terminal repeats, according to the manufacturer's protocol instructions. Briefly, an aliquot (2 μL) of AAV solution was incubated in 18 μL of DNase I at 37 °C for 5 min. After deactivation of DNase at 95 °C for 10 min, an aliquot (2 μL) of the AAV solution was moved to lysis buffer and incubated at room temperature for 3 min. An aliquot (2 μL) of AAV solution was reacted with titre master mix and primer mix at a total volume of 20 μL. Samples were incubated at 95 °C for 10 min and then cycled 30 times at 95 °C for 15 s and then 62 °C for 1 min using a QuantStudio 3 PCR system (Applied Biosystems). For each sample, normalized titre was calculated by dividing the measured titre in each sample by the titre of the AAV solution initially used to resuspend OPO (initial AAV titre = 4.90×10^{10} GC per mL). Each measurement was repeated 3 times ($n = 3$), save for the 144 h time point, which was repeated 2 times ($n = 2$).

2.6.2. AAV distribution assay. AAV-loaded OPO samples were prepared in syringes as described in Section 2.3.1. To assess the uniformity of the AAVs within the syringes, a sample of AAV-loaded OPO was divided into separate parts of approximately equal volume, labelled as segments A, B, and C. Each collected segment was transferred to an Eppendorf tube and immediately stored at −80 °C. Immediately before analysis, the collected AAV-loaded OPO samples were thawed at room temperature and subsequently heated to 95 °C until the OPO fluidized (5–10 min). An aliquot (2 μL) from each segment was analysed to evaluate the final AAV titre using a qPCR AAV Titre Kit (Applied Biological Materials Inc, Cat. No. G931), according to the manufacturer's protocol instructions as described in Section 2.6.1. For each sample, normalized titre was calculated by dividing the measured titre in each sample by the titre of the AAV solution initially used to resuspend OPO (initial AAV titre = 4.90×10^{10} GC per mL). Each measurement was repeated 3 times ($n = 3$).

2.7. ARPE-19 transduction assay

For these studies, AAVs (AAV2-CAG-mGL-BC29) were purchased from PackGene. Prior to shipment, AAVs were characterized using transmission electron microscopy, SDS-PAGE, SYBR Green qPCR, ddPCR, and capillary electrophoresis. AAVs were additionally tested for mycoplasma and thermophilic bacteria and fungi. All AAVs were stored in 1X PBS (pH 7.4) without any additives.

ARPE-19 cells (ATCC, CRL-2302) were thawed into a T25 flask (Nunc, ThermoFisher Scientific) and maintained in DMEM: F-12 Medium (5 mL, ATCC, 30-2006) with 10% fetal bovine serum. At passage 25, cells were seeded to a 12-well microplate and grown to confluency.

Cells were treated either with AAVs (20 μL, $\sim 3 \times 10^{11}$ GC per mL, $n = 3$), AAV-loaded OPO material (20 μL, $\sim 3 \times 10^{11}$ GC per mL AAVs, 14% OPO, $n = 6$), or left untreated ($n = 3$). Cells were incubated at 37 °C, 5% CO_2. After 48 h, cells were imaged using an Echo Revolve fluorescence microscope.

Fluorescent images were analysed using the ImageJ software.[43] Briefly RGB images were converted to 16-bit images. The threshold of each image was adjusted so that all fluorescent cells were highlighted, and images were converted to black and white using the "Make Binary" function. Overlapping cells were separated using the "Watershed" function. Fluorescent cells were counted using the "Anlayze Particles" function, and fluorescent intensity was determined by measuring the mean grey value of each image. Fluorescent cells were additionally counted manually in Adobe Illustrator.

2.8. Photographs and videos

All photographs and videos were recorded using an iPhone 15 Pro Max with original default settings unless otherwise indicated.

2.9. Statistical analyses

Statistical analyses were performed using the OriginLab software. The Student's t-test with a two-tailed distribution was used to compare differences in measured relative mass of FITC-dextran dye released with and without a backing layer, to compare differences in measured AAV titres in AAV-loaded OPO, and to compare differences in mean grey values and cell counts. Results were reported by a significance criterion (p value) and considered statistically significant when $p \leq 0.05$.

3. Results and discussion

3.1. Synthesis and characterization of OPO

The structure of OPO is shown in Scheme 1 in Section 2.2.1. OPO molecules contain poly(ethylene glycol) chains ($n = \sim 227$) capped at either end with octadecane molecules. Our initial attempts to synthesize OPO suffered from issues with reproducibility. In response, we added a preliminary lyophilization step to remove water from the starting reagents. Following this addition, we were able to reproducibly synthesize OPO. After purification, OPO was stored as a white powder, as shown in Fig. 1 in Section 2.3.1.

Since our intention is to use OPO to deliver therapeutics *in vivo*, we added a sterilization step at the end of our synthetic procedure. We preferred the method of sterilizing by submicron filtration over other techniques due to our ability to

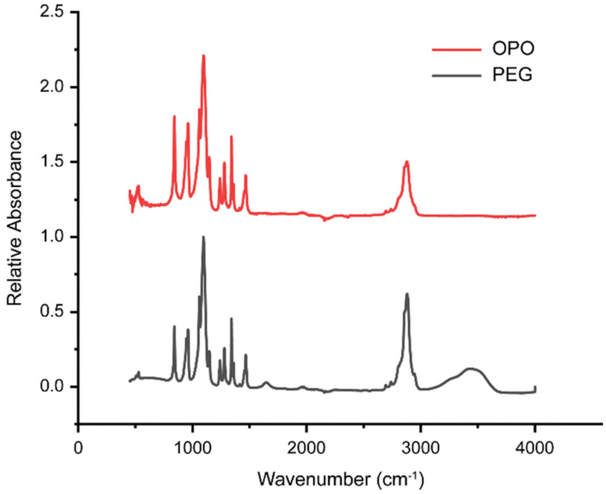

Fig. 4 FTIR-ATR spectra of poly(ethylene glycol) ("PEG", black) and OPO (red). Samples were analysed as solids on a diamond crystal.

Table 1 Characterization of OPO molecular weight and dispersity

	M_n (kg mol^{-1})	M_w (kg mol^{-1})	Đ
Nominal	11		
NMR	11		
SEC	13	14	1.08

filter large amounts of OPO at one time without degrading the OPO polymers. After sterilization, we measured product yields of ~30% OPO. After filtration, we observed no growth in both aerobic and anaerobic media after a 2-week period and concluded that our sterilization protocol was effective.

We characterized the chemical composition of OPO using IR spectroscopy, as shown in Fig. 4. In the IR spectrum, the lack of an O–H stretching band in OPO at ~3300 cm^{-1} confirmed effective substitution of the hydroxyl groups on poly(ethylene glycol).

We additionally characterized OPO using NMR and SEC (see SI for spectra and chromatogram), as summarized in Table 1. Effective substitution of the hydroxyl groups was reinforced by NMR measurements. The molecular weight measured using NMR agreed with the expected nominal mass of OPO, indicating successful synthesis. Dispersity measured by SEC (Đ = 1.08) showed a narrow distribution of molecular weights for our synthesized polymers.

3.2. Preparation and characterization of telechelic network formed by OPO

OPO is a telechelic molecule with a long hydrophilic body capped by hydrophobic moieties on either end. In aqueous solution, the hydrophobic heads associate into micellular-like structures. As the concentration of OPO increases, these micelles become linked by the poly(ethylene glycol) bodies, forming an interconnected, three-dimensional network, as shown in Fig. 5. Individual OPO strands can additionally dangle or form self-loops that are elastically ineffective, or form flower micelles that are external to the larger network.

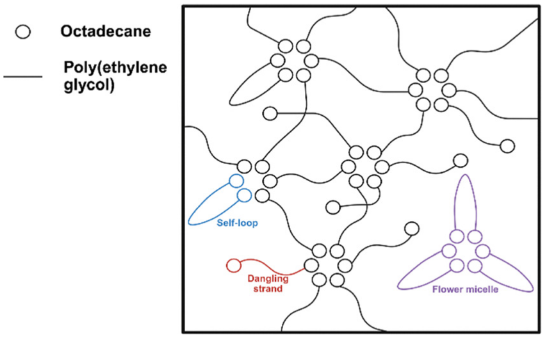

Fig. 5 Schematic drawing of telechelic OPO network. Circles represent octadecane and lines represent poly(ethylene glycol). Examples of a flower micelle (purple), self-loop (blue), and dangling strand (red) are labelled.

In their report detailing synthesis of OPO, Annaka *et al.*[32] resuspended OPO at concentrations ranging from 0–25% in water. They qualitatively evaluated the dependence of phase on concentration and temperature by inverting the resuspended OPO in a vial. At room temperature, they observed a transparent solution at OPO concentrations below ~10%, and a transparent gel at OPO concentrations ranging from 10–25%.

To form an associative network, we resuspended OPO in PBS solutions. Fig. 6 shows our OPO material resuspended at 8%, 14%, 20%, and 26%. At 20% and 26%, the material is not transparent, fragments easily, and cannot be manually injected through an 18G needle. At 8% and 14%, the OPO material is transparent and shows viscoelastic properties. For example, the material does not migrate on inversion for 20 min. After 20 min, 8% OPO begins to flow, while 14% OPO remains in place (see Video in SI). On injection, the material is spreadable, enabling facile deposition onto a target surface (see Video in SI).

Since the material prepared with 14% OPO showed qualitative properties favourable for *in vivo* delivery applications, we further characterized OPO resuspended at this concentration. We evaluated the mechanical properties of the OPO network using frequency-sweep rheological measurements. Previously reported investigations into the rheological properties of OPO examined materials at concentrations of 25% OPO in water.[32] Those investigations found that at 25% OPO, the material is a gel, with the storage modulus larger than the loss modulus over

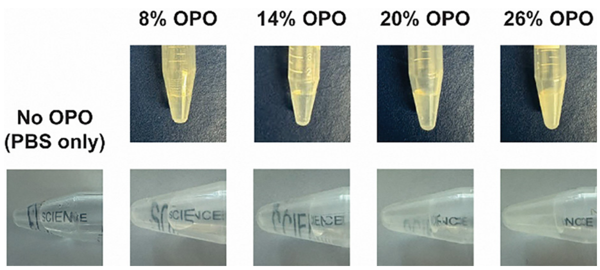

Fig. 6 Photographs of 8%, 14%, 20%, and 26% OPO material. Transparency is demonstrated by holding the material over the word "SCIENCE". A photograph of PBS without OPO is included for reference.

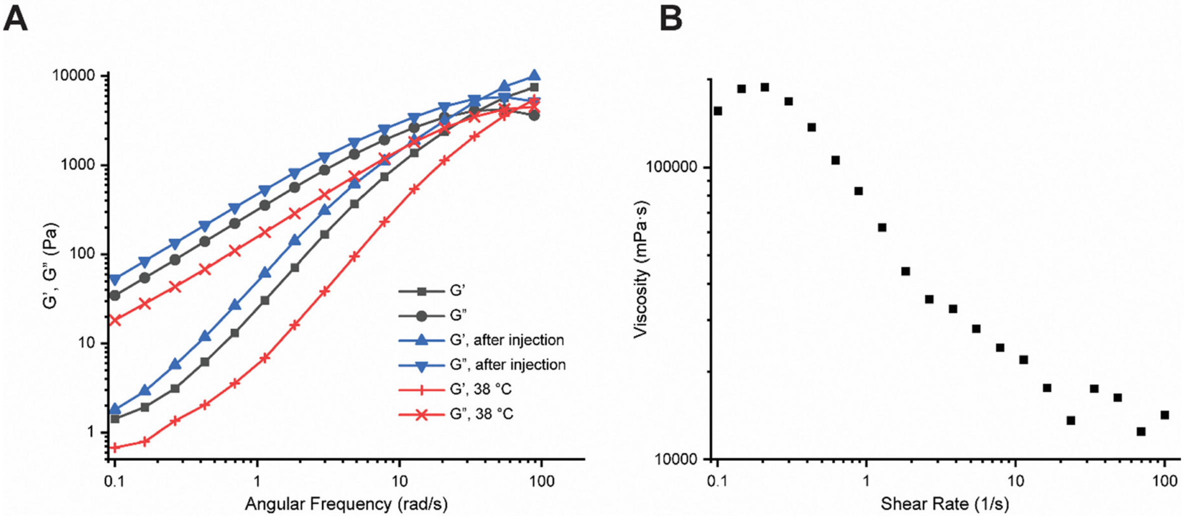

Fig. 7 (A) Frequency-sweep rheology (0.5 mm plate gap, γ = 1%, 0.1–100 rad s^{-1}) of 14% OPO in 1X PBS at room temperature (black), after injection through an 18G needle (blue), and at 38 °C (red). Elastic storage moduli (G') and viscous loss moduli (G'') for each sample are denoted in the legend. (B) Viscosity *versus* shear rate. Shear rate was ramped logarithmically from 0.1–100 s^{-1}.

a frequency range of 0.1–100 s^{-1}. Fig. 7A shows the frequency-sweep measurements of our 14% OPO in PBS.

Frequency-sweep rheology indicates that our 14% OPO is a viscoelastic fluid. Over the frequencies measured, the OPO material showed Maxwellian behaviour, with primarily elastic behaviour ($G' > G''$) at shorter timescales, viscous behaviour ($G'' > G'$) at longer timescales, and a finite crossover frequency indicating a single relaxation time. Importantly, these properties have been observed for other telechelic materials formed by chemically similar, micelle-forming polymers, and thus reinforce the network model indicated in Fig. 5.[20,36,44,45]

These properties are further consistent with transient networks formed by dynamic crosslinks.[20,46,47] At room temperature, the OPO molecules that link micellular structures into a network are constantly exchanged. These dynamic linkages enable the OPO material to be deformed and spread while retaining loaded agents. We further hypothesized that on injection, the network structure collapses, causing the OPO material to fluidize and pass through a needle. Then, on exiting the needle, the network structure reforms, and the OPO material retains loaded agents.

To evaluate this hypothesis, we first measured the viscosity of our OPO material with changing shear rate. As shown in Fig. 7B, there is a small amount of low-shear thickening. This behaviour has been observed in other telechelic materials, and is likely caused by chain stretching and recapture.[48] At higher shear rates, there is significant shear thinning, indicating fluidization of the material as the network structure collapses.

We verified that the OPO network structure reforms after fluidization by measuring the frequency-sweep rheology after injection through an 18G needle. As shown in Fig. 7A, the frequency-sweep rheological properties are consistent after injection. Importantly, the OPO material showed the same Maxwellian behaviour before and after injection, suggesting that the dynamic, telechelic network structure is present in both instances. The preservation of loaded agents after injection will be discussed further in Section 3.3 and is demonstrated on video (see Video in SI).

We further evaluated the rheological properties of the OPO material at body temperature. As shown in Fig. 7A, at 38 °C the frequency-sweep behaviour is shifted rightward, reflecting the expected decrease in relaxation time with increasing temperature for a dynamically linked network.[44,47] The preservation of Maxwellian behaviour indicates that the network structure remains intact despite the increase in temperature.

Though numerous models exist that aim to quantitate the rheological behaviour of telechelic materials, these models frequently rely on phenomenological parameters, and a comprehensive understanding of the molecular mechanisms that occur in these materials remains elusive.[20,36,44,46,49–51] Future investigations will further interrogate these parameters by measuring how properties like polymer concentration[36,44,52] and length of the hydrophobic end groups[49,50] impact the rheological behaviour of our material.

However, the rheological measurements presented here demonstrate certain properties that are essential for our intended application to deliver retinal gene therapies. The OPO material is formed by a telechelic network, where elastic associations break and reform. On injection, the material fluidizes, enabling it to be pushed through a needle, allowing for facile deposition onto the retinal surface. After injection, the network structure reforms and is maintained at body temperature, ensuring preservation of loaded agents.

3.3. Dissolution of and release from telechelic OPO network

To evaluate efficacy for delivery applications, we monitored both the dissolution of the OPO network, and release of loaded agents from the OPO network over time. The OPO material can be deposited either by scooping and spreading onto a surface, or through injection. In bulk solution, the OPO adheres to plastic, glass, and *ex vivo* retinal tissue, even while under mild agitation (see Videos in SI).

As aforementioned in Section 3.2, the OPO network is held together by dynamic, hydrophobic interactions. In bulk solution, the network takes in water and swells. Concurrently, OPO polymer strands become detached from the network and dissolve into the bulk solution. The network structure collapses after a critical number of polymer strands dissolve.

The OPO network remains visually intact for 40–50 min in bulk solution. As shown in Fig. 8A, we quantified dissolution of the OPO network by monitoring the concentration of OPO polymer strands in bulk solution over time. These measurements

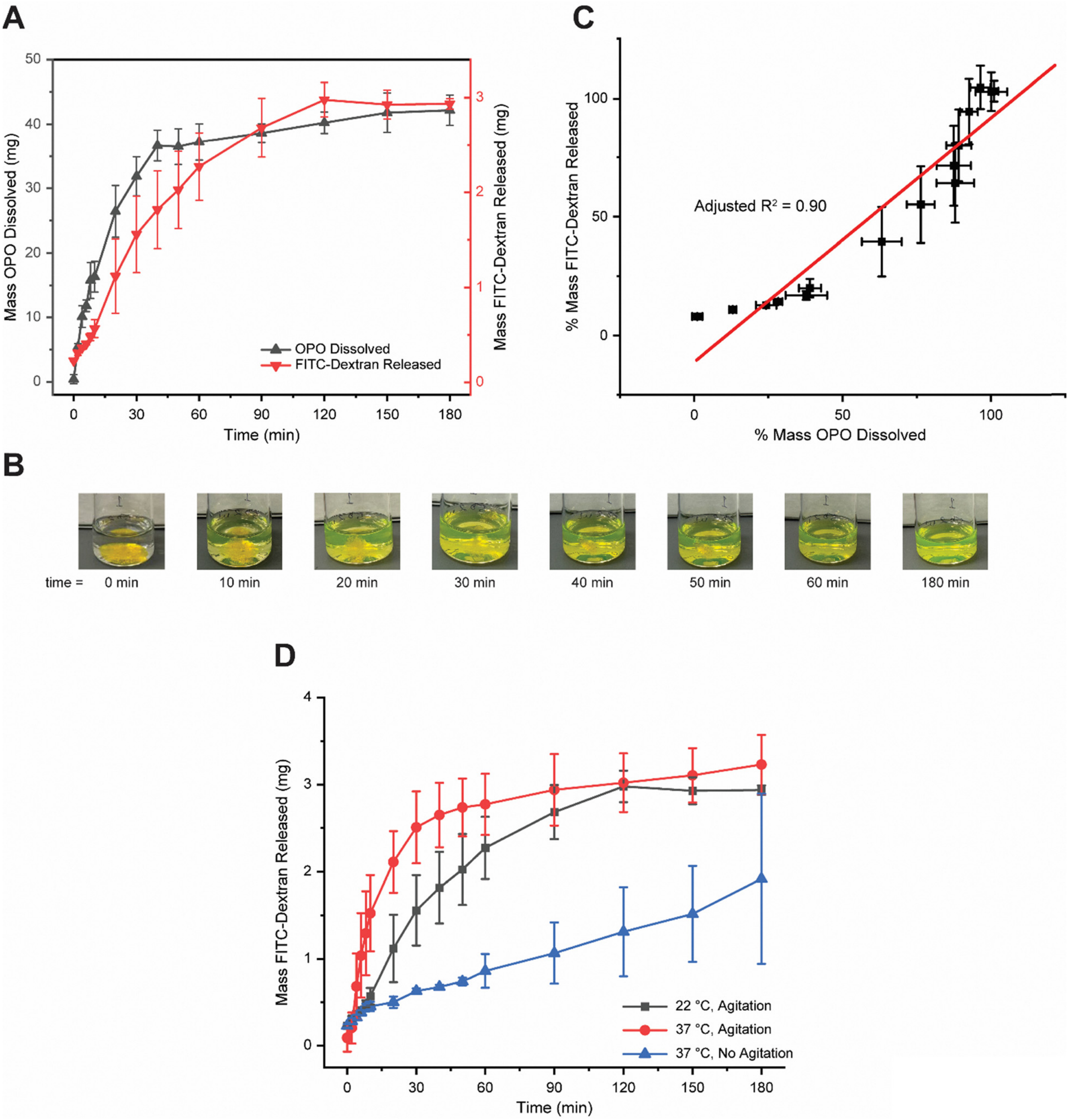

Fig. 8 (A) Dissolution of OPO (left axis, black, upward triangles) and release of FITC-dextran from OPO network (right axis, red, downward triangles) over 180 min at room temperature. OPO was placed in PBS and gently agitated at room temperature. At each time point, an aliquot of the bulk solution was collected. Mass of OPO dissolved and mass of FITC-dextran released were determined by measuring OPO absorbance and FITC-dextran fluorescence, respectively, in each aliquot. (B) Photographs of release of FITC-dextran from the OPO network over a period of 0 to 180 min. (C) Comparison of percent OPO mass dissolved and percent FITC-dextran mass released. Percent mass was calculated by dividing the mass measured at each time point by the mass measured after 24 h. (D) Release of FITC-dextran from OPO network over 180 min at 37 °C with agitation (red circles) and without agitation (blue triangles). The release data from 8A (black squares, labelled "22 °C, Agitation") is reprinted for comparison. Error bars represent standard deviations (n = 3).

generally agree with qualitative observations. For 40 min, the mass of OPO polymer strands lost from the network to the bulk solution gradually increases. After 40 min, the mass of dissolved OPO plateaus, corresponding with the visual dissolution of the network.

We selected FITC-dextran dye with a molecular weight of 2 MDa as a model to monitor release of loaded agents from the OPO network. At this molecular weight, the hydrodynamic radius of FITC-dextran ($\sim$30 nm) is comparable to that of AAV vectors, and thus simulates diffusion of viruses that are commonly used to mediate retinal gene therapy.[53,54] Additionally, FITC-dextran is facilely detected through fluorescence measurements. We loaded FITC-dextran into the OPO network by resuspending OPO in 20 mg mL^{-1} dye solutions. We injected loaded OPO into vials, incubated the loaded OPO in PBS, and evaluated release of dye from the OPO network into the bulk solution over time. Fig. 8A and B show the release of FITC-dextran from the OPO network over time.

As shown in Fig. 8A, most FITC-dextran dye is retained in the OPO material after injection into a vial (t = 0 min). FITC-dextran is then increasingly released from the OPO network for $\sim$60 min. After 60 min, the release plateaus. This is similar to the measured dissolution of the OPO network and suggests that dissolution of OPO is an important factor driving release of loaded agents.

We additionally compared the dissolution and release rates, as shown in Fig. 8C. Percent mass of OPO dissolved and percent mass of FITC-dextran released were determined by dividing the mass measured at each time point by the mass measured after incubation for 24 h. The linear relationship (adjusted R^2 = 0.90) reinforces our understanding that dissolution of the OPO network drives the release of loaded agents. As OPO strands dissolve, the material becomes more fluid-like, and loaded agents are increasingly eluted from the liquid phase into the surrounding environment.

Since dissolution of OPO drives release of loaded agents, temperature and agitation may impact the release profile from the OPO material. For example, elevated temperature and increased agitation generally increase the rate of dissolution and thus may increase the rate of release from the OPO material. To better understand how the OPO material will behave *in vivo* we monitored release of FITC-dextran dye at 37 °C both with and without agitation on a mixer. As shown in Fig. 8D, compared to samples that were agitated at room temperature, samples agitated at 37 °C released loaded agents more rapidly. When the samples were not agitated, the initial rate of release decreased $\sim$6.5-fold. In both cases, the OPO material retained $>$90% of loaded cargo after injection and remained visibly intact for $>$30 min. *In vivo* intraocular temperatures are generally less than 37 °C,[55] and, while difficult to quantify, we expect agitation on the retinal surface to be less than that caused by a mixer operating at 250 rpm. Thus, we expect the release profile *in vivo* to be somewhere in between the curves presented in Fig. 8D.

These results indicate that OPO is well-positioned to deliver AAV vectors. The network remains intact for over 30 min, enabling deposition onto the retinal surface. The material is facilely deposited *via* injection, retains loaded agents on injection, and remains adhesive even under agitation. Over time, the network dissolves, releasing loaded agents into the surrounding environment.

3.4. OPO backing layer

As the OPO network dissolves, loaded agents diffuse radially in all directions. We hypothesized that control over the direction of release could be enhanced by placing an unloaded OPO material backing layer behind OPO loaded with delivery agents.

As described in Section 2.5, to evaluate this hypothesis, we developed a two-chamber sample holder. A circular cell connected the two chambers in the centre. OPO loaded with FITC-dextran dye was deposited onto one window of the cell, while OPO with no loaded agent was deposited onto the opposing window, such that both layers were touching. For control measurements ("no backing layer"), OPO loaded with FITC-dextran dye was deposited onto each window. Each chamber was filled with PBS, and PBS was able to pass between chambers through the cell containing OPO. We evaluated release of FITC-dextran by sampling from each chamber over time and measuring FITC-dextran fluorescence. Fig. 9A and B show the mass of dye released into each chamber with and without an unloaded backing layer, respectively.

At early time points, there is negligible release of dye into either chamber. After 150 min, dye begins to diffuse into the chambers. When a backing layer is included, the dye preferentially diffuses into the chamber opposite the backing layer, and there is a larger difference in the mass of dye between each chamber. Contrarily, when there is no backing layer, dye diffuses into both chambers, and the difference in mass between chambers is smaller.

After the initial release of dye, we observed large standard deviations in the average relative mass of dye released, indicating variability in the measurements. We hypothesize that this variability is the result of the system equilibrating. At 240 min, the standard deviations decreased. At this point, when a backing layer was included, we measured a statistical difference in the relative mass of dye in either chamber (p = 0.049). When a backing layer was not included, we did not measure a statistical difference between chambers (p = 0.496). This difference is further reflected in the photographs shown in Fig. 9C. When a backing layer is included, after 240 min, the chamber opposite the backing layer is visibly more yellow, indicating the presence of more dye. When a backing layer is not included, both chambers are yellow. After several hours, both chambers are yellow regardless of the inclusion of a backing layer. This corresponds with dissolution of the material and confirms that buffer and dye were able to travel between chambers.

It should be noted that these measurements do not fully align with the results of the release assay reported in Section 3.3. In addition to a longer period of equilibration, the OPO network remained intact longer during the backing layer experiments. We attribute these differences to differences in the experimental setup. In Section 3.3, loaded OPO was incubated in bulk buffer. In contrast, here the OPO was deposited in

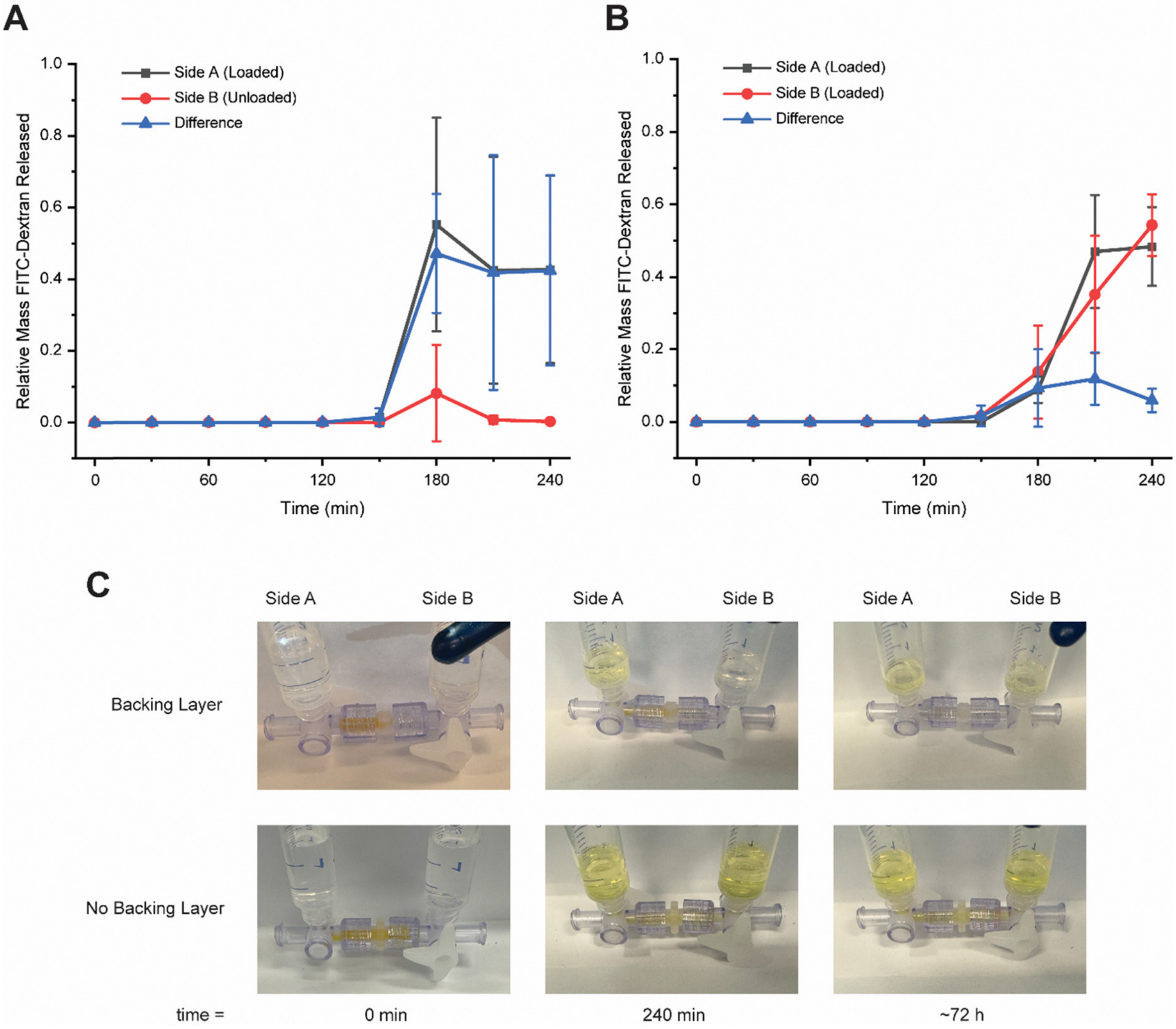

Fig. 9 Relative mass of FITC-dextran dye released from OPO material into sample chambers over time (A) with and (B) without an unloaded backing layer. For experiments with a backing layer, OPO loaded with FITC-dextran was injected on the left side ("Side A") and unloaded OPO was injected on the right side ("Side B") of the sample cell. For experiments without a backing layer, OPO loaded with FITC-dextran dye was injected on both sides of the sample cell. PBS was deposited into each chamber, and the two-chamber setup was gently agitated. Aliquots were collected from each chamber at each time point. FITC-dextran mass was determined by measuring FITC-dextran fluorescence in each aliquot. The relative mass of FITC-dextran in Side A (black squares), Side B (red circles), and the difference (blue triangles) are reported. Relative mass was calculated by dividing the mass measured at each time point by the sum of the masses measured in both chambers after 72 hours. Error bars represent standard deviations (n = 3). (C) Photographs of the chambers with and without a backing layer at 0 min, 240 min, and 72 h.

a sample cell, and only a fraction of its surface ($\sim$12.6 mm^2) was exposed to bulk PBS. Additionally, the unloaded OPO backing layer partially blocked exposure of the loaded layer to the bulk PBS. This reduced exposure to the bulk solution could explain the additional time needed to reach equilibrium, and the extended lifetime of the OPO network. These results additionally suggest that in practice, an unloaded material backing layer could extend the duration of release of loaded agents from the OPO material.

These results indicate that placement of an unloaded OPO backing layer behind a loaded OPO layer promotes unidirectional diffusion away from the backing layer. In practice, a backing layer could be placed on top of a loaded layer to enhance release of loaded agents towards the retina. This would enable more localized release, reducing the amount of therapeutics necessary for effective treatment.

3.5. Stability and distribution of AAVs in OPO network

Adeno-associated viruses (AAVs) are a family of viruses that have been identified as promising candidates to transduce genes to retinal cells, mediating retinal gene therapy.[56,57] To further demonstrate the feasibility of using OPO to deliver retinal gene therapies, we prepared OPO loaded with AAVs, and investigated the properties of AAV-loaded OPO.

AAV-loaded OPO was prepared as described in Section 2.3.1. Briefly, OPO was diluted to a concentration of 14% with AAV solution in a syringe. The mixture was then centrifuged until the OPO was resuspended into a transparent material. We prepared

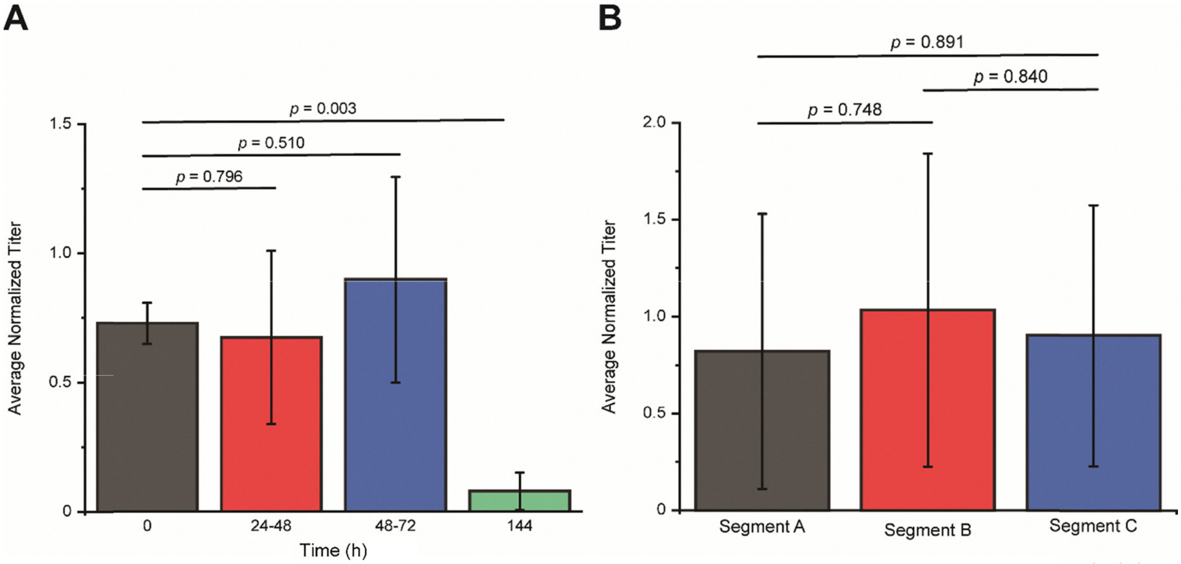

Fig. 10 Average normalized viral titre in OPO loaded with AAVs (A) over time and (B) in different segments collected from a single OPO sample. AAV-loaded OPO was prepared as described in Section 2.3.1. Viral titre was measured in aliquots from each sample using a qPCR AAV Titre Kit. For time-dependent studies, AAV titre was measured immediately after preparation (t = 0 h), and after 24, 48, and 144 h. In between timepoints, AAV-loaded OPO was stored at 4 °C. For segmentation studies, AAV-loaded OPO was prepared and segments were collected from different sections of the OPO. AAV titre in each segment was then measured. Each measured titre was normalized by dividing by the titre of the AAV solution used to prepare the AAV-loaded OPO samples. Comparative statistics are reported by a significance criterion (p value). Error bars indicate standard deviations (n = 2 for t = 144 h measurements; n = 3 for all other measurements).

OPO material with viral titres on the order of $\sim 10^{10}$ GC per mL. At these titres, there was a sufficient amount of AAVs in the OPO material aliquots to measure stability and distribution of AAVs using a qPCR titre kit. As shown in Fig. 10, we measured the stability and distribution of AAVs in the resuspended OPO network. To enable comparison between samples, measured titres were normalized by the titre of AAV solution used to initially resuspend the OPO samples.

Fig. 10A shows the measured AAV titres in OPO over time. AAV titre was first measured immediately after preparation of the AAV-loaded OPO (t = 0 h). Subsequently, titre was measured after 24, 48, and 144 h. In between measurements, AAV-loaded OPO was stored at 4 °C. For the first 72 h, the average AAV titres were of the same order of magnitude as that measured at t = 0 h and showed no statistically significant differences ($p \geq 0.510$). This indicates that the AAV titre was stable inside the OPO over this period. At t = 144 h, the measured titre decreased by an order of magnitude. It should be noted that due to loss of sample with each measurement, only 2 measurements were collected for t = 144 h. However, we observed a statistically significant reduction in average titre for t = 144 h compared to that at t = 0 h (p = 0.003), indicating that AAVs had degraded or had become stuck to the syringe the material was stored in.

These results suggest that AAVs are stable after loading into OPO for up to at least 3 days, so long as the samples are stored at 4 °C. In practice, the AAV-loaded OPO can be prepared in advance of a surgical protocol and still deliver the same AAV titre as immediately prepared samples.

It has been observed that AAVs adsorb to surfaces such as glass and plastic.[58,59] This is problematic for clinical applications, as AAVs stored in syringes may adsorb to the surface of the syringe, reducing the AAV titre administered to patients. The results here indicate that the AAV titre in OPO is stable for 3 days, despite storage in a plastic syringe. We hypothesize that the OPO network may limit contact of AAVs with the surface of the syringe, inhibiting adsorption. Thus, AAV-loaded OPO can be prepared and stored in a syringe up to 3 days prior to application without reduction in AAV titre.

Fig. 10B shows the measured AAV titres collected from different segments of AAV-loaded OPO. The average titres between segments were of the same order of magnitude and showed no statistically significant differences ($p \geq 0.748$), suggesting that the AAVs had been homogeneously distributed throughout the OPO network.

We have demonstrated our ability to facilely prepare OPO material loaded with AAVs. AAV-loaded OPO was prepared in the same way as OPO loaded with FITC-dextran dye. After fabrication, we demonstrated that AAVs are homogeneously distributed throughout the OPO network. Thus, clinicians can reliably estimate the AAV titre administered to a patient from the initial titre of AAV loaded into OPO and the administered volume of AAV-loaded OPO. Our results indicate that AAV titre in OPO is further stable for at least 3 days, enabling flexibility with respect to sample preparation and shipment before administration. OPO may additionally shield loaded AAVs from adsorption, enabling preparation in syringes without reduction in titre. These properties well-position OPO to deliver retinal gene therapies in clinical settings. In future studies, we will investigate the behaviour of AAV-loaded OPO at various temperatures to further validate the results reported here. We will additionally develop and refine a surgical protocol for administering AAV-loaded OPO *in vivo*.

3.6. ARPE-19 transduction assay

To further evaluate the efficacy of using OPO material to administer AAVs to the retina, we administered AAV-loaded OPO material to ARPE-19 cells. ARPE-19 is a human retinal epithelium cell line that is frequently used to study retinal gene therapies.[60,61]

AAV transduction was evaluated by monitoring green fluorescent protein expression in ARPE-19 cells after incubation with AAVs for 48 h. Fig. 11A shows fluorescent images of cells treated with an equivalent amount of AAVs administered either in PBS ("AAV only") or in OPO material ("AAV-loaded OPO material"). The vibrant fluorescence in samples treated with OPO confirms our ability to administer transducing AAVs with OPO material.

We further analysed the fluorescent images using the software ImageJ. Fluorescence intensity was quantified by measuring the mean grey value of each image. As shown in Fig. 11B, images of samples treated with OPO material ("AAV-loaded OPO material") showed mean grey values greater than 0, confirming the ability of OPO material to deliver transducing AAVs. However, the mean grey value of samples treated with OPO material was less than that of images of samples treated with AAVs administered in PBS ("AAV Only", p = 0.050). We hypothesize that this reduction in mean grey value is an artifact

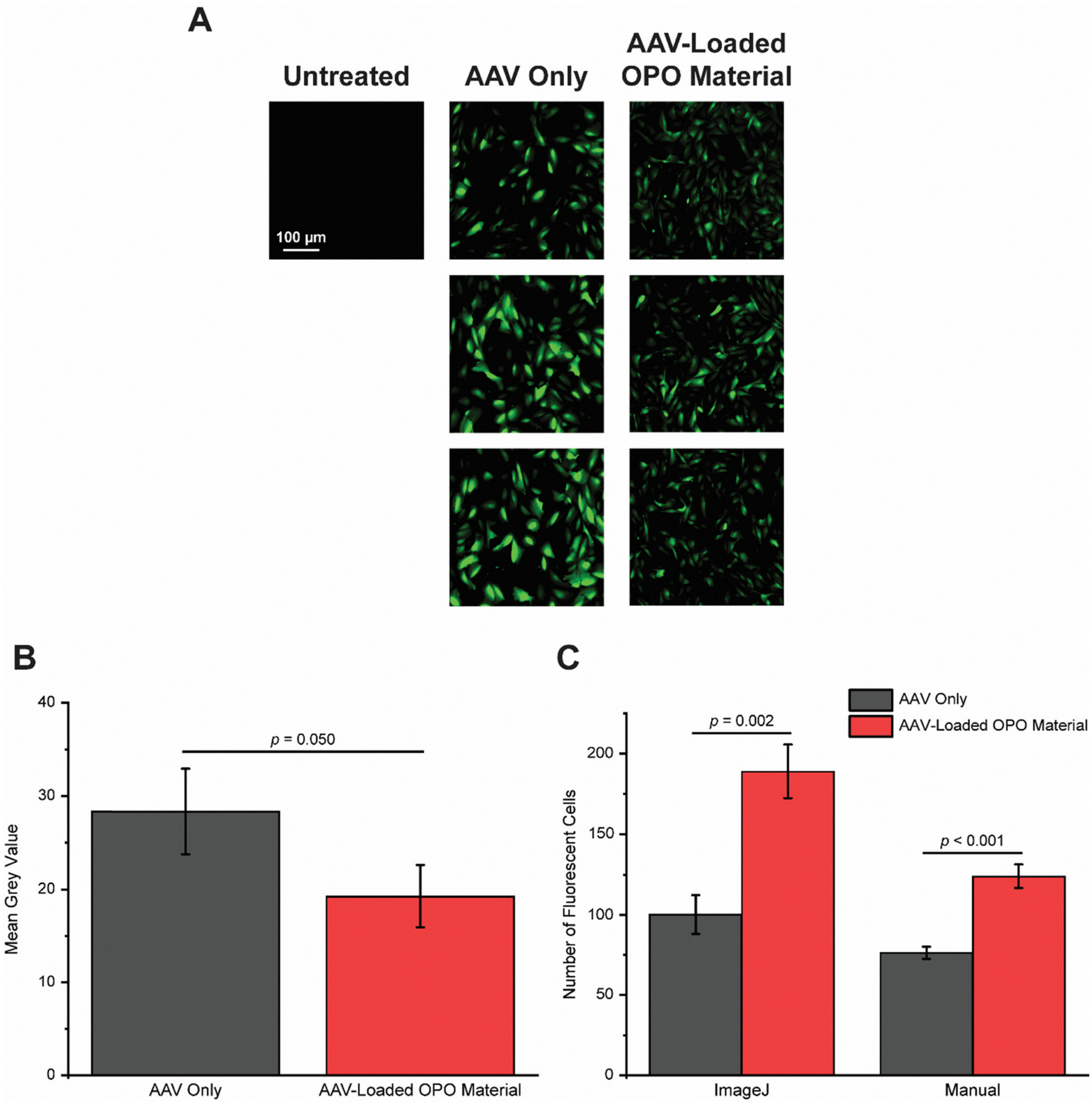

Fig. 11 (A) Green fluorescent protein expression in ARPE-19 cells treated with no AAVs ("untreated"), AAVs administered in PBS ("AAV only"), and AAVs administered in OPO material ("AAV-loaded OPO material"). (B) Average mean grey value of fluorescent images. (C) Average number of fluorescent cells in images counted using ImageJ and manually in Adobe Illustrator. Error bars indicate standard deviations (n = 3).

of our experimental setup. For these experiments, we utilized 12-well microplates. Thus, as the OPO material dissolved, residual OPO was confined to the well. This residual OPO may have interfered with the fluorescence imaging, thus decreasing the measured intensity of fluorescence. We do not expect this to occur *in vivo* as dissolved OPO will be refluxed away from the retina.

To further evaluate how the OPO material impacts AAV transducability, we counted the number of fluorescent cells in each image. We first utilized the ''Watershed'' function in ImageJ to separate overlapping cells in each image.[62] However, due to the abnormal circularity of ARPE-19 cells, we found that the ImageJ software sometimes separated single cells into multiple fragments. To alleviate this error, we supplemented our analysis in ImageJ by manually counting fluorescent cells using the software Adobe Illustrator (see SI). As shown in Fig. 11C, whether counted in ImageJ or manually, images of samples treated with OPO material contained more fluorescent cells than images of samples treated with AAVs administered in PBS. This indicates that OPO material can be used to administer AAVs with enhanced transducability.

It has been reported that synthetic materials can diminish the reliability of *ex vivo* cell assays.[63] The studies reported herein suffered from additional artifacts that may mask the full benefit of our delivery approach. For example, cells were confined to a well, immersed in media, and not subject to reflux, thus minimizing the impact of the adhesive and protective properties of the OPO material we would expect to observe *in vivo*. Nevertheless, here we have shown that OPO material can be used to administer transducing AAVs. These results serve as a crucial foundation as we move to fully assess the efficacy of our materials-based delivery strategy using *in vivo* models.

4. Conclusions

We report the development of a novel material formed by OPO molecules. In aqueous solution, the hydrophobic heads on the polymers associate into micelles *via* hydrophobic interactions, forming an interconnected telechelic network. The material shows Maxwellian properties, with dynamic associations that break and reform. These properties are consistent before and after injection through a needle, and at room and body temperature, enabling facile application of the OPO material both *in vitro* and *in vivo*.

When OPO is resuspended in a solution that contains delivery agents, those agents become trapped in the network structure. In bulk solution, the network gradually dissolves, concurrently releasing loaded agents. Placement of an unloaded backing layer next to a loaded layer promotes unidirectional release away from the backing layer and may prolong the duration of release.

We envision using this OPO material for the delivery of AAV-based retinal gene therapies. The material can be facilely loaded with viral vectors and administered onto the retinal surface *via* injection without a complex surgery. Localized delivery onto the retina would reduce dosing, increase transduction efficiency, and lower surgical risks and immunogenicity. The material would additionally prevent reflux of therapeutics to non-targeted areas of the eye, improving efficiency and reducing the risk of vector induced intraocular inflammation. These advantageous properties could be further enhanced by incorporation of an unloaded material backing layer.

These properties may prove helpful for other delivery applications. For example, the OPO material can be spread over surfaces, and thus may be useful in localizing delivery of therapeutics to skin wounds. Here, we have extensively characterized OPO and demonstrated properties compelling for *in vivo* applications. Importantly, we have demonstrated that our OPO material is injectable and retains loaded agents after passing through a needle, uniquely positioning it to deliver therapeutics to the eye. To our knowledge, this is the first report of an injectable material that has been loaded with retinal gene therapies and thus is a crucial preliminary step in advancing a materials-based strategy for administering gene therapies to the retina. Next, we plan to evaluate efficacy of the OPO material to deliver retinal gene therapies using *in vivo* models.

We are additionally evaluating how systematic alterations to the composition of OPO impact its mechanical properties and release profile. For example, increasing the size of the hydrophobic end groups may reduce dissolution of the network and prolong release of loaded agents, but additionally make the material more gel-like and difficult to inject. These systematic investigations may prove useful in tuning the properties of OPO for other delivery applications.

Author contributions

James H. Westbay: conceptualization, formal analysis, investigation, methodology, validation, visualization, writing – original draft, writing – review & editing. Daniel P. Bigley: conceptualization, formal analysis, investigation, methodology, validation, writing – review & editing. Sushma Sappa: conceptualization, formal analysis, investigation, methodology, validation, writing – review & editing. Anfisa Ayalon: conceptualization, writing – review & editing. Hamzah Aweidah: conceptualization, writing – review & editing. Lauren D. Dignam: investigation, writing – review & editing. Joseph N. Martel: conceptualization, funding acquisition, project administration, supervision, writing – review & editing. William A. Beltran: conceptualization, funding acquisition, project administration, supervision, writing – review & editing. José-Alain Sahel: conceptualization, funding acquisition, project administration, supervision, writing – review & editing. Leah C. Byrne: conceptualization, funding acquisition, project administration, supervision, writing – review & editing. Morgan V. DiLeo: conceptualization, formal analysis, methodology, funding acquisition, project administration, supervision, writing – review & editing.

Conflicts of interest

There are no conflicts to declare.

Data availability

All relevant research data has been included in the manuscript and supplementary information (SI). Supplementary information: calibration curves of OPO absorbance and FITC-dextran fluorescence used to quantify OPO and FITC-dextran in dissolution, release, and backing layer experiments; ^{1}H NMR spectra of 1-bromooctadecane, poly(ethylene glycol), and OPO; size-exclusion chromatogram of OPO; MALDI-MS spectrum of OPO; release assays with smaller OPO volume and AAV-loaded OPO; manual count of fluorescent cells. Videos depicting inversion, injection, agitation, and adhesion of OPO material. See DOI: https://doi.org/10.1039/d6tb00267f.

Acknowledgements

The authors wish to thank Megan Clarke and the Meyer Group for assistance with size-exclusion chromatography and mass spectrometry, and for advice regarding polymer synthesis. The authors also wish to thank Jovina Vaswani and the Velankar Group for assistance with rheological measurements. Work performed in the University of Pittsburgh Dietrich School NMR Core Facility (RRID:SCR_025126) and services and instruments used in this project were graciously supported, in part, by the University of Pittsburgh. Work performed in the University of Pittsburgh Dietrich School Mass Spectrometry Facility (RRID:SCR_025123) and services and instruments used in this project were graciously supported, in part, by the University of Pittsburgh. Work performed in the University of Pittsburgh Dietrich School Materials Characterization Laboratory (RRID:SCR_025127) and services and instruments used in this project were graciously supported, in part, by the University of Pittsburgh. The authors acknowledge the National Institutes of Health (grant no. 5R01EY033049) and U.S. Department of Defense (grant no. MTEC-22-02-MPAI-001) for financial support. This work was also supported by NIH CORE Grant P30 EY08098 to the Department of Ophthalmology, from the Eye and Ear Foundation of Pittsburgh, and from an unrestricted grant from Research to Prevent Blindness, New York, NY. J.H.W. was supported in part by the National Institutes of Health's Interdisciplinary Visual Sciences training program (grant no. 5T32EY017271). Fig. 1, 5, the Table of Contents Fig., and figures in the SI were created in BioRender (https://BioRender.com; Fig. 1: https://biorender.com/ulodwv6; Fig. 5: https://biorender.com/g58t069; Table of Contents: https://biorender.com/5jdhkm5.)

References

1 A. M. Vargason, A. C. Anselmo and S. Mitragotri, The evolution of commercial drug delivery technologies, *Nat. Biomed. Eng.*, 2021, **5**(9), 951–967.

2 D. A. Kuzmin, M. V. Shutova, N. R. Johnston, O. P. Smith, V. V. Fedorin, Y. S. Kukushkin, J. C. M. van der Loo and E. C. Johnstone, The clinical landscape for AAV gene therapies, *Nat. Rev. Drug Discovery*, 2021, **20**(3), 173–174, DOI: 10.1038/d41573-021-00017-7.

3 R. A. Bush, Y. Zeng, P. Colosi, S. Kjellstrom, S. Hiriyanna, C. Vijayasarathy, M. Santos, J. Li, Z. Wu and P. A. Sieving, Preclinical dose-escalation study of intravitreal AAV-RS1 gene therapy in a mouse model of X-linked retinoschisis: dose-dependent expression and improved retinal structure and function, *Hum. Gene Ther.*, 2016, **27**(5), 376–389.

4 F. L. Brodie, J. Ruggiero, D. H. Ghodasra, J. Z. Hui, B. L. VanderBeek and A. J. Brucker, Volume and composition of reflux following intravitreal injection, *Retina*, 2014, **34**(7), 1473.

5 S. G. Jacobson, A. V. Cideciyan, R. Ratnakaram, E. Heon, S. B. Schwartz, A. J. Roman, M. C. Peden, T. S. Aleman, S. L. Boye and A. Sumaroka, Gene therapy for leber congenital amaurosis caused by RPE65 mutations: safety and efficacy in 15 children and adults followed up to 3 years, *Arch. Ophthalmol.*, 2012, **130**(1), 9–24.

6 K. Stieger, J. Schroeder, N. Provost, A. Mendes-Madeira, B. Belbellaa, G. Le Meur, M. Weber, J.-Y. Deschamps, B. Lorenz and P. Moullier, Detection of intact rAAV particles up to 6 years after successful gene transfer in the retina of dogs and primates, *Mol. Ther.*, 2009, **17**(3), 516–523.

7 T. K. MacLachlan, M. Lukason, M. Collins, R. Munger, E. Isenberger, C. Rogers, S. Malatos, E. DuFresne, J. Morris and R. Calcedo, Preclinical safety evaluation of AAV2-sFLT01—a gene therapy for age-related macular degeneration, *Mol. Ther.*, 2011, **19**(2), 326–334.

8 S. E. Boye, J. J. Alexander, C. D. Witherspoon, S. L. Boye, J. J. Peterson, M. E. Clark, K. J. Sandefer, C. A. Girkin, W. W. Hauswirth and P. D. Gamlin, Highly efficient delivery of adeno-associated viral vectors to the primate retina, *Hum. Gene Ther.*, 2016, **27**(8), 580–597.

9 W. S. Gange, R. A. Sisk, C. G. Besirli, T. C. Lee, M. Havunjian, H. Schwartz, M. Borchert, J. D. Sengillo, C. Mendoza and A. M. Berrocal, Perifoveal chorioretinal atrophy after subretinal voretigene neparvovec-rzyl for RPE65-mediated leber congenital amaurosis, *Ophthalmol. Retina*, 2022, **6**(1), 58–64.

10 I. P. Seitz, F. Wozar, G. A. Ochakovski, F. F. Reichel, F. Gelisken, K. U. Bartz-Schmidt, T. Peters and M. D. Fischer, Dose-dependent progression of chorioretinal atrophy at the injection site after subretinal injection of rAAV2/8 in nonhuman primates, *Ophthalmol. Sci.*, 2024, **4**(5), 100516.

11 M. D. Fischer, F. Simonelli, J. Sahni, F. G. Holz, R. Maier, C. Fasser, A. Suhner, D. P. Stiehl, B. Chen and I. Audo, Real-world safety and effectiveness of voretigene neparvovec: results up to 2 years from the prospective, registry-based PERCEIVE Study, *Biomolecules*, 2024, **14**(1), 122.

12 V. Kansara, L. Muya, C.-R. Wan and T. A. Ciulla, Suprachoroidal delivery of viral and nonviral gene therapy for retinal diseases, *J. Ocul. Pharmacol. Ther.*, 2020, **36**(6), 384–392.

13 K. Y. Wu, J. K. Fujioka, T. Gholamian, M. Zaharia and S. D. Tran, Suprachoroidal injection: a novel approach for targeted drug delivery, *Pharmaceuticals*, 2023, **16**(9), 1241.

14 R. M. Schek, S. J. Hollister and P. H. Krebsbach, Delivery and protection of adenoviruses using biocompatible hydrogels for localized gene therapy, *Mol. Ther.*, 2004, **9**(1), 130–138.

15 J. Li and D. J. Mooney, Designing hydrogels for controlled drug delivery, *Nat. Rev. Mater.*, 2016, **1**(12), 1–17.

16 M. J. Webber and E. T. Pashuck, (Macro)molecular self-assembly for hydrogel drug delivery, *Adv. Drug Delivery Rev.*, 2021, **172**, 275–295.

17 M. Kato, S. Ishikawa, Q. Shen, Z. Du, T. Katashima, M. Naito, T. Numahata, M. Okazaki, T. Sakai and M. Kurita, In situ-formable, dynamic crosslinked poly (ethylene glycol) carrier for localized adeno-associated virus infection and reduced off-target effects, *Commun. Biol.*, 2023, **6**(1), 508.

18 Z. Han, P. Wang, G. Mao, T. Yin, D. Zhong, B. Yiming, X. Hu, Z. Jia, G. Nian and S. Qu, Dual pH-responsive hydrogel actuator for lipophilic drug delivery, *ACS Appl. Mater. Interfaces*, 2020, **12**(10), 12010–12017.

19 Y. Wu, X. Gu, X. Chen, Y. Cui, W. Jiang and B. Liu, Hydrogel: a new material for intravesical drug delivery after bladder cancer surgery, *J. Mater. Chem. B*, 2024, **12**(12), 2938–2949.

20 T. Katashima, Rheological studies on polymer networks with static and dynamic crosslinks, *Polym. J.*, 2021, **53**(10), 1073–1082.

21 T. Tanigo, R. Takaoka and Y. Tabata, Sustained release of water-insoluble simvastatin from biodegradable hydrogel augments bone regeneration, *J. Controlled Release*, 2010, **143**(2), 201–206.

22 X. Jin, C.-x Wei, C.-w Wu and W. Zhang, Customized hydrogel for sustained release of highly water-soluble drugs, *ACS Omega*, 2022, **7**(10), 8493–8497.

23 T. V. Chirila and Y. Hong, Poly (1-vinyl-2-pyrrolidinone) hydrogels as vitreous substitutes: a rheological study, *Polym. Int.*, 1998, **46**(3), 183–195.

24 S. Schnichels, N. Schneider, C. Hohenadl, J. Hurst, A. Schatz, K. Januschowski and M. S. Spitzer, Efficacy of two different thiol-modified crosslinked hyaluronate formulations as vitreous replacement compared to silicone oil in a model of retinal detachment, *PLoS One*, 2017, **12**(3), e0172895.

25 V. Pertici, C. Pin-Barre, C. Rivera, C. Pellegrino, J. Laurin, D. Gigmes and T. Trimaille, Degradable and injectable hydrogel for drug delivery in soft tissues, *Biomacromolecules*, 2018, **20**(1), 149–163.

26 H.-S. Kim, J. Yang, K. Kim and U. S. Shin, Biodegradable and injectable hydrogels as an immunosuppressive drug delivery system, *Mater. Sci. Eng. C*, 2019, **98**, 472–481.

27 P. Sheikholeslami, B. Muirhead, D. S. H. Baek, H. Wang, X. Zhao, D. Sivakumaran, S. Boyd, H. Sheardown and T. Hoare, Hydrophobically-modified poly (vinyl pyrrolidone) as a physically-associative, shear-responsive ophthalmic hydrogel, *Exp. Eye Res.*, 2015, **137**, 18–31.

28 W.-F. Lai, Development of hydrogels with self-healing properties for delivery of bioactive agents, *Mol. Pharmaceutics*, 2021, **18**(5), 1833–1841.

29 P. Bertsch, M. Diba, D. J. Mooney and S. C. Leeuwenburgh, Self-healing injectable hydrogels for tissue regeneration, *Chem. Rev.*, 2022, **123**(2), 834–873.

30 C. A. Dreiss, Wormlike micelles: where do we stand? Recent developments, linear rheology and scattering techniques, *Soft Matter*, 2007, **3**(8), 956–970.

31 S. R. Raghavan and J. F. Douglas, The conundrum of gel formation by molecular nanofibers, wormlike micelles, and filamentous proteins: gelation without cross-links?, *Soft Matter*, 2012, **8**(33), 8539–8546.

32 M. Annaka, K. Mortensen, M. E. Vigild, T. Matsuura, S. Tsuji, T. Ueda and H. Tsujinaka, Design of an injectable in situ gelation biomaterials for vitreous substitute, *Biomacromolecules*, 2011, **12**(11), 4011–4021.

33 R. Kumar, G. C. Kalur, L. Ziserman, D. Danino and S. R. Raghavan, Wormlike micelles of a C22-tailed zwitterionic betaine surfactant: from viscoelastic solutions to elastic gels, *Langmuir*, 2007, **23**(26), 12849–12856.

34 M. Cates and S. Candau, Statics and dynamics of worm-like surfactant micelles, *J. Phys.: Condens. Matter*, 1990, **2**(33), 6869.

35 K. Tam, R. Jenkins, M. Winnik and D. Bassett, A structural model of hydrophobically modified urethane– ethoxylate (HEUR) associative polymers in shear flows, *Macromolecules*, 1998, **31**(13), 4149–4159.

36 S. Suzuki, T. Uneyama and H. Watanabe, Concentration dependence of nonlinear rheological properties of hydrophobically modified ethoxylated urethane aqueous solutions, *Macromolecules*, 2013, **46**(9), 3497–3504.

37 T. Guan, Z. Du, J. Peng, D. Zhao, N. Sun and B. Ren, Polymerizable hydrophobically modified ethoxylated urethane acrylate polymer: synthesis and viscoelastic behavior in aqueous systems, *Macromolecules*, 2020, **53**(17), 7420–7429.

38 J.-F. Berret and Y. Séréro, Evidence of shear-induced fluid fracture in telechelic polymer networks, *Phys. Rev. Lett.*, 2001, **87**(4), 048303.

39 H. Teles, T. Vermonden, G. Eggink, W. Hennink and F. de Wolf, Hydrogels of collagen-inspired telechelic triblock copolymers for the sustained release of proteins, *J. Controlled Release*, 2010, **147**(2), 298–303.

40 M. Arslan, D. Aydin, A. Degirmenci, A. Sanyal and R. Sanyal, Embedding well-defined responsive hydrogels with nanocontainers: tunable materials from telechelic polymers and cyclodextrins, *ACS Omega*, 2017, **2**(10), 6658–6667.

41 S. Hoshi, F. Okamoto, T. Murakami, T. Sakai, Y. Shinohara, T. Fujii, M. Nakatani and T. Oshika, Ability of nonswelling polyethylene glycol-based vitreous hydrogel to maintain transparency in the presence of vitreous hemorrhage, *Transl. Vis. Sci. Technol.*, 2019, **8**(6), 33.

42 K. Hayashi, F. Okamoto, S. Hoshi, T. Katashima, D. C. Zujur, X. Li, M. Shibayama, E. P. Gilbert, U.-I. Chung and S. Ohba, Fast-forming hydrogel with ultralow polymeric

content as an artificial vitreous body, *Nat. Biomed. Eng.*, 2017, **1**(3), 0044.

43 C. A. Schneider, W. S. Rasband and K. W. Eliceiri, NIH Image to ImageJ: 25 years of image analysis, *Nat. Methods*, 2012, **9**(7), 671–675.

44 T. Uneyama, S. Suzuki and H. Watanabe, Concentration dependence of rheological properties of telechelic associative polymer solutions, *Phys. Rev. E: Stat., Nonlinear, Soft Matter Phys.*, 2012, **86**(3), 031802.

45 Q. Pham, W. Russel, J. Thibeault and W. Lau, Micellar solutions of associative triblock copolymers: The relationship between structure and rheology, *Macromolecules*, 1999, **32**(15), 5139–5146.

46 M. Ohnishi, T. Katashima, M. Nakahata and O. Urakawa, Relationships between diffusion and viscoelasticity of associative polymer networks, *Nihon Reoroji Gakkaishi*, 2019, **47**(4), 133–142.

47 T. Katashima, R. Kudo, M. Naito, S. Nagatoishi, K. Miyata, U.-I. Chung, K. Tsumoto and T. Sakai, Experimental comparison of bond lifetime and viscoelastic relaxation in transient networks with well-controlled structures, *ACS Macro Lett.*, 2022, **11**(6), 753–759.

48 S. X. Ma and S. L. Cooper, Shear thickening in aqueous solutions of hydrocarbon end-capped poly (ethylene oxide), *Macromolecules*, 2001, **34**(10), 3294–3301.

49 N. Sanabria-DeLong, S. K. Agrawal, S. R. Bhatia and G. N. Tew, Impact of synthetic technique on PLA– PEO– PLA physical hydrogel properties, *Macromolecules*, 2007, **40**(22), 7864–7873.

50 S. K. Agrawal, N. Sanabria-DeLong, S. K. Bhatia, G. N. Tew and S. R. Bhatia, Energetics of Association in Poly(lactic acid)-based hydrogels with crystalline and nanoparticle– polymer junctions, *Langmuir*, 2010, **26**(22), 17330–17338.

51 I. W. Hamley, G. Cheng and V. Castelletto, A thermoresponsive hydrogel based on telechelic PEG end-capped with hydrophobic dipeptides, *Macromol. Biosci.*, 2011, **11**(8), 1068–1078.

52 R. Tanaka, J. Meadows, G. Phillips and P. Williams, Viscometric and spectroscopic studies on the solution behaviour of hydrophobically modified cellulosic polymers, *Carbohydr. Polym.*, 1990, **12**(4), 443–459.

53 S. De Smedt, T. K. Meyvis, J. Demeester, P. Van Oostveldt, J. Blonk and W. E. Hennink, Diffusion of macromolecules in dextran methacrylate solutions and gels as studied by confocal scanning laser microscopy, *Macromolecules*, 1997, **30**(17), 4863–4870.

54 J. K. Armstrong, R. B. Wenby, H. J. Meiselman and T. C. Fisher, The hydrodynamic radii of macromolecules and their effect on red blood cell aggregation, *Biophys. J.*, 2004, **87**(6), 4259–4270.

55 K. Shinoda, S. C. Matsumoto, K. Yagura, G. Terauchi, T. Shoji, Y. Yoshikawa, Y. Igawa, A. Mizota and Y. Miyake, Intraocular temperature distribution in eyes undergoing different types of surgical procedures during vitreous surgery, *J. Clin. Med.*, 2022, **11**(7), 2053.

56 L. C. Byrne, T. P. Day, M. Visel, J. A. Strazzeri, C. Fortuny, D. Dalkara, W. H. Merigan, D. V. Schaffer and J. G. Flannery, In vivo–directed evolution of adeno-associated virus in the primate retina, *JCI Insight*, 2020, **5**, 10.

57 B. E. Öztürk, M. E. Johnson, M. Kleyman, S. Turunç, J. He, S. Jabalameli, Z. Xi, M. Visel, V. L. Dufour and S. Iwabe, scAAVengr, a transcriptome-based pipeline for quantitative ranking of engineered AAVs with single-cell resolution, *eLife*, 2021, **10**, e64175.

58 J. Sanmiguel, G. Gao and L. H. Vandenberghe, Quantitative and digital droplet-based AAV genome titration, *Adeno-Associated Virus Vectors: Design and Delivery*, 2019, pp. 51–83.

59 A. Srivastava, K. M. Mallela, N. Deorkar and G. Brophy, Manufacturing challenges and rational formulation development for AAV viral vectors, *J. Pharm. Sci.*, 2021, **110**(7), 2609–2624.

60 K. Dunn, A. Aotaki-Keen, F. Putkey and L. Hjelmeland, ARPE-19, a human retinal pigment epithelial cell line with differentiated properties, *Exp. Eye Res.*, 1996, **62**(2), 155–170.

61 D. Gurtsieva, E. Minskaia, S. Zhuravleva, E. Subcheva, E. Sakhibgaraeva, A. Brovin, A. Tumaev and A. Karabelsky, Engineered AAV2. 7m8 serotype shows significantly higher transduction efficiency of ARPE-19 and HEK293 cell lines compared to AAV5, AAV8 and AAV9 serotypes, *Pharmaceutics*, 2024, **16**(1), 138.

62 J. He, M. Kleyman, J. Chen, A. Alikaya, K. M. Rothenhoefer, B. E. Ozturk, M. Wirthlin, A. C. Bostan, K. Fish and L. C. Byrne, Transcriptional and anatomical diversity of medium spiny neurons in the primate striatum, *Curr. Biol.*, 2021, **31**(24), 5473–5486.e5476.

63 R. Podgórski, M. Wojasiński and T. Ciach, Nanofibrous materials affect the reaction of cytotoxicity assays, *Sci. Rep.*, 2022, **12**(1), 9047.